Journal of Computational Physics 247 (2013) 208–227

Contents lists available at SciVerse ScienceDirect

Journal of Computational Physics

journal homepage: www.elsevier.com/locate/jcp

Development of a wavenumber-preserving scheme for solving Maxwell's equations in curvilinear non-staggered grids

Tony W.H. Sheu [a,b,c,*], C.M. Mei [a], J.H. Li [a]

[a] Department of Engineering Science and Ocean Engineering, National Taiwan University, No. 1, Section 4, Roosevelt Road, Taipei, Taiwan, ROC
[b] Taida Institute of Mathematical Science (TIMS), National Taiwan University, Taiwan, ROC
[c] Center of Advanced Study in Theoretical Sciences (CASTS), National Taiwan University, Taiwan, ROC

ARTICLE INFO

Article history:
Received 12 October 2011
Received in revised form 25 February 2013
Accepted 23 March 2013
Available online 12 April 2013

Keywords:
Maxwell's equations
Curvilinear coordinates
Non-staggered grids
Zero-divergence
Fourth-order
Dual-preserving solver
Numerical scaled wavenumber error

ABSTRACT

In this paper a compact finite-difference solver for solving the Maxwell's equations in curvilinear coordinates is presented. The scheme formulated in time domain can theoretically preserve zero-divergence condition and scaled wavenumber characteristics in non-staggered grids. The inherent local conservation laws are also retained discretely all the time. The space and time derivative terms are approximated to yield an equal fourth-order spatial and temporal accuracy. In irregular physical domain, Maxwell's equations are recast in terms of the contravariant and covariant field variables so that the developed dual-preserving solver can be directly implemented. In addition, in curvilinear coordinates the four components in the metric tensor have been calculated under the guideline that the determinant of the transformation matrix is computed exactly. Through the computational exercises, it is demonstrated that the newly proposed solver with a fairly small numerical scaled wavenumber error in curvilinear coordinates is computationally efficient for use to get the long time accurate Maxwell's solutions in irregular physical domain.

© 2013 Elsevier Inc. All rights reserved.

1. Introduction

Provided that the constraint conditions $\nabla \cdot \underline{B} = 0$ and $\nabla \cdot \underline{D} = 0$ are imposed initially, the divergence-free equations for $\underline{B}$ (magnetic flux density) and $\underline{D}$ (electric flux density) in Maxwell's equations are preserved all the time by means of the time-evolving Faraday's and Ampère's laws. In other words, the Gauss' law for the magnetism and electricity can be left out of consideration when solving the values of $\underline{B}$ and $\underline{D}$ from the Faraday's and Ampère's laws, respectively. The discrete divergence-free conditions for the magnetism and electricity are not satisfied in general due to the inevitably introduced discretization error. Violation of these two constraint equations for the magnetic and electric flux densities can even result in numerical instability problem. How to eliminate these non-zero divergence errors when simulating the Maxwell's equations becomes, thus, one of the major tasks in the development of numerical methods for solving the Maxwell's equations. One can refer to the book of Birdsall and Langdon [1] for getting more information about the numerical control of divergence errors of $\underline{B}$ and $\underline{D}$. In this study, two divergence-free-preserving algorithms will be investigated in Section 3.

Control of divergence errors is particularly essential when solving the Maxwell's equations since any accumulated non-zero divergence error can cause the calculation to breakdown [2]. To enforce divergence-free constraint conditions in Maxwell's equations, one can employ the well known Yee's scheme [3] in staggered grids. The generalized Lagrange

* Corresponding author at: Department of Engineering Science and Ocean Engineering, National Taiwan University, No. 1, Section 4, Roosevelt Road, Taipei, Taiwan, ROC. Tel.: +886 2 33665746; fax: +886 2 23929885.
E-mail address: twhsheu@ntu.edu.tw (T.W.H. Sheu).

0021-9991/$ - see front matter © 2013 Elsevier Inc. All rights reserved.
http://dx.doi.org/10.1016/j.jcp.2013.03.062

multiplier formulation of Munz et al. [4] is another class of numerical methods developed to retain divergence-free conditions for the Maxwell's equations. The local divergence-free solution of Maxwell's equations can be also computed using the discontinuous Galerkin method [5].

Numerical errors of the amplitude or the phase type will inevitably appear when approximating the derivative terms. The resulting dissipation error can attenuate solution amplitude and the dispersion error can lead to an even worse erroneous numerical phase or group velocity. Since Maxwell's equations contain only the first-order spatial derivative terms, the indispensable numerical dispersion error can destabilize the scheme. It is therefore essential to reduce this type of errors when approximating the first-order spatial derivative terms. How to preserve the embedded propagation characteristics in the Maxwell's equations is the second challenge of getting an accurate numerical solution.

A trivial way to reduce the dissipation and dispersion errors resulting from the approximation of derivative terms is to adopt the high-order schemes such as the spectral method [6,7]. Application of this class of methods is, however, limited to problems in simple domains subject to less complex boundary conditions. The other alternative to spectral methods is the methods developed on the basis of Pade' approximation [8]. This class of compact schemes offers high-order approximations to differential operators using the compact stencils that relate various derivatives with the nodal values of dependent variables under calculation. Compared to the traditional finite difference methods, a better representation of the shorter length scale can be obtained using the spectral methods. There has, however, a larger freedom in prescribing the boundary condition along the irregular boundary [9]. Due to the spectral-like resolution properties in compact schemes, the sixth-order accurate scheme for the first-order spatial derivative terms in time-domain Maxwell's equations in Section 6.3 and the Jacobian-preserving scheme developed in Section 6.1 for calculating the metric tensor components will be developed within the context of compact finite difference methods.

To eliminate the dissipation error entirely, the centered compact scheme is chosen to get a dissipation-free solution. It has been known that in non-staggered grids the centered compact scheme employed for approximating the first-order spatial derivative terms might cause numerical oscillations to occur even for the conditions without involving discontinuity in the solution. To resolve this oscillatory problem without adding dissipation or filter to the dissipation-free centered compact scheme, in this study a dispersively accurate scheme described in Section 6.3 is proposed so that the difference between the numerical and exact wavenumbers for the first-order spatial derivative term becomes smallest.

Discretization error is basically cumulative. After solving the EM wave equations for a long distance or for a long time, the time-evolving solution will be greatly affected by the scheme which can not preserve the multisymplectic geometric structure. Moreover, the predicted solution can be unphysical since the local conservation laws can no longer be preserved. How to retain the embedded symplecticity in the Maxwell's equations in large-scale problem or for a problem involving a long-term computation poses another difficulty in approximating the time derivative terms shown in the Faraday's and Ampère's equations.

It is well known that given a numerical scheme for the partial differential equations the solution with the best numerical quality is normally computed from a domain of Cartesian grids. This computational fact prompts the calculation of the transformed differential equations in the computational domain cast in a form akin to that in Cartesian coordinate counterpart. In this study, the Maxwell's equations formulated in curvilinear coordinates employ the contravariant and covariant field variables described in Section 4 so that the temporal and spatial schemes derived in the Cartesian coordinates can be applied directly to get a better solution without the sacrifice of the crosswind diffusion error. The coefficients in these transformed equations become, however, more complex in their expressions containing the components of metric tensor. It is therefore essential to accurately compute these terms resulting from the transformation between the physical and computational coordinates. In Section 6.1, a Jacobian-preserving scheme formulated within the compact finite different framework is proposed to get not only a more accurate representation of the metric tensor components but also a more accurate area ratio between the physical and computational cells.

The rest of this paper is organized as follows. In Section 2, the Maxwell's equations which include the Faraday's law for the time-evolving magnetic flux density and the Ampère's law for the time-evolving electric flux density are presented. These two sets of equations will be solved subject to the Gauss' laws for the solenoidal magnetism and electricity. In Section 3, we present two divergence-free algorithms for the Gauss' law. In Section 4, the Maxwell's equations in physical domain are mapped one-to-one to those in the computational domain. The electric and magnetic field variables are transformed to their corresponding contravariant and covariant components. In Section 5, Maxwell's equations in perfectly matched layer are presented in Cartesian as well as in curvilinear coordinates. In Section 6, the first-order spatial derivative terms shown in the Maxwell's equations are approximated in a way that the numerical scaled wavenumber error is minimized. Since Maxwell's equations are classified to be a set of multisymplectic Hamiltonian partial differential equations [10], we apply a fourth-order accurate symplectic structure-preserving time integrator to implicity conserve its symplecticity numerically. We also present in the same section a detailed analysis of our scheme in Fourier space. In Section 7, one problem with the exact solution is solved to verify the proposed fourth-order space/time accurate scheme, which accommodates the zero-divergence-preserving and symplecticity-preserving properties, with the smallest numerical wavenumber error. Finally, we draw some conclusions in Section 7 based on the solutions computed from the Maxwell's equations in an irregular domain.

2. Working equations

The following Maxwell's equations in time domain are investigated to get the magnetic field intensity $\underline{H}$ and the electric field intensity $\underline{E}$

$$\frac{\partial \underline{H}}{\partial t} = -\frac{1}{\mu}\nabla \times \underline{E}, \tag{1}$$

$$\frac{\partial \underline{E}}{\partial t} = \frac{1}{\epsilon}\nabla \times \underline{H}. \tag{2}$$

The magnitudes of ϵ (electric permittivity) and μ (magnetic permeability) shown above determine the wave propagation speed $c(\equiv (\varepsilon\mu)^{1/2})$. We assume that the permeability in Faraday's law and the permittivity in Ampère's law are homogeneous and isotropic. These two material parameters are the proportional constants in the linear isotropic constitutive relations $\underline{D} = \epsilon\underline{E}$ and $\underline{B} = \mu\underline{H}$, where $\underline{B}$ and $\underline{D}$ are denoted as the magnetic induction (or magnetic flux density) and electric displacement (or electric flux density), respectively. While Maxwell's equations can be decomposed into the transverse magnetic (TM) and the transverse electric (TE) modes, only the TM-mode Maxwell's equations are considered in this study for brevity.

Provided that there are no electric and magnetic sources, analysis of the transport equations for $\underline{H}$ and $\underline{E}$ should be constrained by the following Gauss' laws for magnetism and electricity, respectively

$$\nabla \cdot \underline{B} = 0, \tag{3}$$

$$\nabla \cdot \underline{D} = 0. \tag{4}$$

Note that Eqs. (3) and (4) are satisfied if they are both divergence-free initially [5]. This implies that we can neglect these two divergence-free equations only in the context of continuous differential equations.

Maxwell's equations (1) and (2) can be reformulated to the equivalent set of mutltisymplectic Hamiltonian equations $\overset{\mathrm{M}}{=}\underline{z}_t + \sum_{k=1}^{3}\overset{\mathrm{K_k}}{=}\underline{z}_k = \nabla_z S(\underline{z})$ for the solution vector $\underline{z} = (Hx, Hy, Hz, Ex, Ey, Ez)^T$, skew symmetric matrix $\overset{\mathrm{M}}{=}$, symplectic structure $\overset{\mathrm{K_k}}{=}$ $(k = 1\text{—}3)$, and the energy functional $S(\underline{z})$ [11]. By virtue of the local energy conservation law, the total energy conservation law for the Maxwell's equations is

$$\int_\Omega \left(\frac{1}{\epsilon}\underline{H}\cdot\nabla\times\underline{H} + \frac{1}{\mu}\underline{E}\cdot\nabla\times\underline{E}\right)d\Omega = \int_\Omega \left(\underline{H}\cdot\frac{\partial E}{\partial t} - \underline{E}\cdot\frac{\partial H}{\partial t}\right)d\Omega. \tag{5}$$

In other words, equations (1)–(4) are endowed with the following Hamiltonian functional H [12]

$$H(\underline{H},\underline{E}) = \frac{1}{2}\int_\Omega \left(\frac{1}{\epsilon}\underline{H}\cdot\nabla\times\underline{H} + \frac{1}{\mu}\underline{E}\cdot\nabla\times\underline{E}\right)d\Omega. \tag{6}$$

Besides the above two available conservation laws, Maxwell's equations (1) and (2) have the following two additional invariants

$$W_1(t) = \int_\Omega (\epsilon\underline{E}\cdot\underline{E} + \mu\underline{H}\cdot\underline{H})d\Omega, \tag{7}$$

$$W_2(t) = \int_\Omega \left(\epsilon\left|\frac{\partial\underline{E}}{\partial t}\right|^2 + \mu\left|\frac{\partial\underline{H}}{\partial t}\right|^2\right)d\Omega. \tag{8}$$

The first invariant, or $W_1(t)$, is the energy density in the field of electromagnetism.

3. Divergence-free-preserving solution algorithm

There are six unknown field variables shown in the differential set of eight Eqs. (1)–(4), which include three equations in Faraday's law for $\underline{B}$, three equations in Ampère's law for $\underline{D}$, and two equations in Gauss' law for magnetism and electricity. To close this dynamical system, we need only six of the eight equations. This leaves the two elliptic Eqs. (3) and (4) out of consideration. Omission of these two divergence-free equations can very often result in a serious numerical stability problem. We are therefore motivated to modify Eqs. (1) and (2) and then solve them in time domain. The resulting computed solutions satisfy Eqs. (3) and (4) or the Gauss' laws all the time. In this study we propose two methods and assess their performance in terms of the divergence-free numerical errors and the required computational times.

To ensure satisfaction of the Gauss' law in a discrete sense, two potential functions Φ_1 and Φ_2 have been introduced into Eqs. (2) and (1), respectively, to get the following modified Ampère's and Faraday's equations [13,1].

$$\frac{\partial\underline{E}}{\partial t} - \frac{1}{\epsilon}\nabla\times\underline{H} + \nabla\Phi_1 = 0, \tag{9}$$

$$\frac{\partial\underline{H}}{\partial t} + \frac{1}{\mu}\nabla\times\underline{E} + \nabla\Phi_2 = 0. \tag{10}$$

To close the above set of modified Maxwell's equations, two transport equations for modeling the correction potentials Φ_1 and Φ_2 need to be derived. Define first the differential operators D_1 and D_2 for the Gauss' law and then rewrite the modified Gauss' law as follows

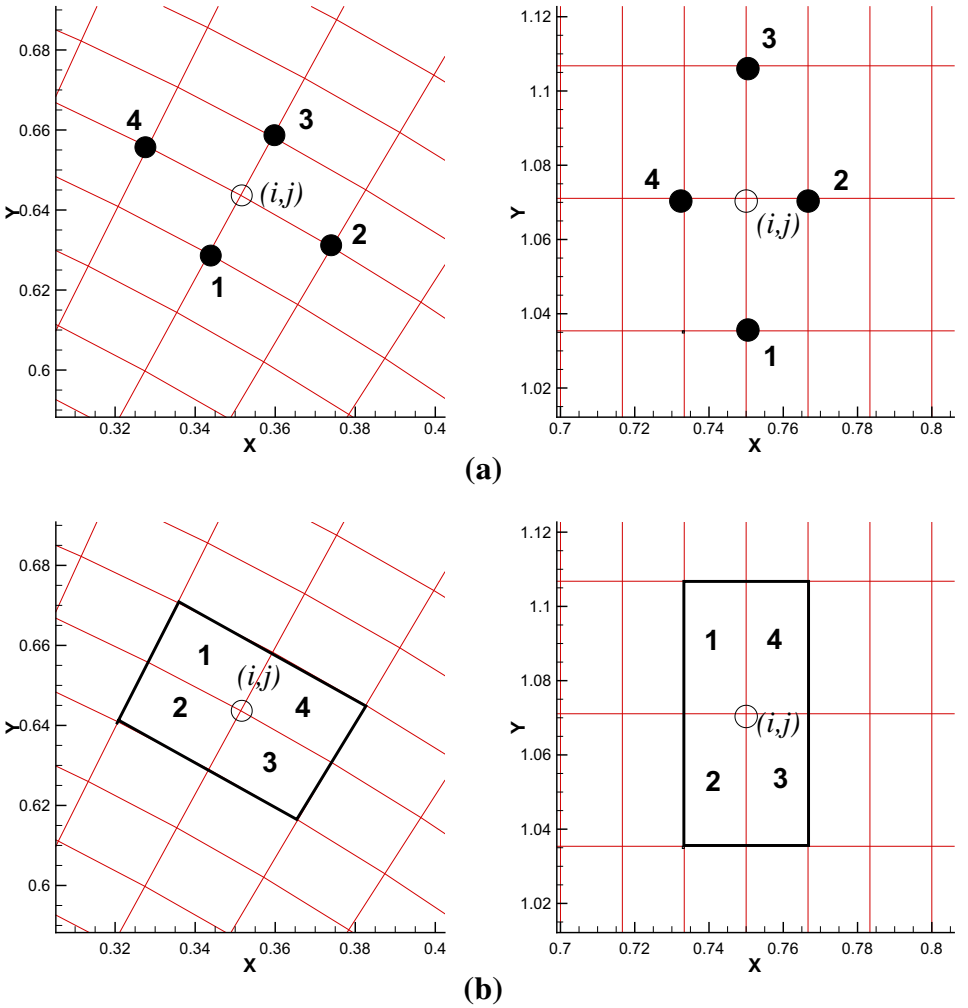

Fig. 1. (a) Schematic of interior cells in physical and computational domains with the nodes $1, 2, 3, 4$; (b) Schematic of the four areas marked by $1, 2, 3, 4$ in a cell.

$$D_1\Phi_1 + \nabla \cdot \underline{E} = 0, \tag{11}$$

$$D_2\Phi_2 + \nabla \cdot \underline{H} = 0. \tag{12}$$

By performing the divergence operator $(\nabla\cdot)$ on Eq. (9) and then the differential operator $\partial/\partial t$ on Eq. (11), the equation for Φ_1 can be derived as follows

$$\frac{\partial D_1(\Phi_1)}{\partial t} - \nabla^2\Phi_1 = -\frac{1}{\epsilon}\nabla \cdot (\nabla \times \underline{H}). \tag{13}$$

Since $D_1\Phi_1 = -\nabla \cdot \underline{E}$, we can get

$$\nabla^2\Phi_1 = -\frac{\partial}{\partial t}(\nabla \cdot \underline{E}). \tag{14}$$

For the two-dimensional case without considering the current density and electric charge density, the equation governing the correction function Φ_1 turns out to be the Laplace equation $\nabla^2\Phi_1 = 0$. One can similarly perform the divergence operator $(\nabla\cdot)$ on Eq. (10) and the differential operator $\partial/\partial t$ on Eq. (12). The following transport equation for Φ_2 can be derived through the identity equation $\nabla \cdot (\nabla \times \underline{E}) = 0$

$$\nabla^2\Phi_2 = -\frac{\partial}{\partial \mathrm{t}}(\nabla \cdot \underline{H}). \tag{15}$$

One can also express the computed electrical field vector as the sum of $-\nabla\phi$ and $\nabla \times \underline{V}$, where ϕ denotes a scalar function and $\underline{V}$ is a vector function. Decomposition of the solution in this way permits us to correct the electrical field by means of $\underline{E}_c = \underline{E} + \nabla\phi$ and this helps to make the corrected vector $\underline{E}_c$ to be solenoidal. By performing the divergence operator $(\nabla\cdot)$ on both hand sides of $\underline{E}_c = \underline{E} + \nabla\phi_E$, we can get the following equation for the correction term in Ω

$$\nabla^2\phi_E = -\nabla\cdot\underline{E}. \tag{16}$$

Given the computed values of $\underline{E}$ from the Faraday's equations, the above equation for ϕ is solved subject to the zero boundary condition $\phi = 0$ along the boundary $\partial\Omega$ since the Lagrangian multiplier is simply used to enforce divergence-free condition. Note that ϕ_E is prescribed to be zero along the boundary since its primary role is to ensure numerical stability [14]. One can adopt the similar correction idea by adding $\nabla\phi_H$ to the magnetic field solution $\underline{E}$ computed from the Ampère's law, where ϕ_H is governed by $\nabla^2\phi_H = -\nabla\cdot\underline{H}$ in Ω and $\phi_H = 0$ is prescribed along $\partial\Omega$.

4. Maxwell's equations in curvilinear coordinates

To simulate the EM wave propagation over a geometrically complex electromagnetic structure, we can transform the Maxwell's equations, governed by Eqs. (9) and (10) in Cartesian coordinates $x^i (i = 1{-}3)$, to their corresponding equations in a non-orthogonal curvilinear coordinate system $\xi^i (i = 1{-}3)$. In an irregular physical domain, mesh lines are not necessarily orthogonal to each other. The mesh sizes can also vary considerably from one region to the other. It is therefore essential to solve the transformed equations more accurately in a computationally best orthogonal and uniform grid system. Provided that a coordinate transformation is performed, the transformed equations become much more complex by the space derivative terms generated from the coordinate transformation. For the sake of retaining solution accuracy as that predicted in Cartesian coordinates without deteriorating convergence when solving the Maxwell's equations in nonuniform curvilinear meshes, one should choose a proper set of dependent variables for the investigated magnetic and electric field variables. In this study, we transform equations (1) and (2) to their equivalent equations cast in both covariant and contravariant components for $\underline{E}$ and $\underline{H}$.

Given a vector $\underline{v} = v_i$, which is $\underline{E}$ *or* $\underline{H}$ in the Maxwell's equations, it can be expressed either in the covariant basis vector $\underline{e}_{(i)} \left(\equiv \frac{\partial x}{\partial \xi^i}\right)$ form or in the contravariant basis vector $e^{(i)} \left(\equiv \frac{\partial \xi^i}{\partial x}\right)$ form by $\underline{v} = V^i\, \underline{e}_{(i)} = V_i \underline{e}^{(i)}$. Note that V^i are denoted as the contravariant components of $\underline{v}$ along the covariant basis vector that is tangential to $\underline{v}$. On the contrary, V_i are denoted as the covariant components of $\underline{v}$ along the contravariant basis vector that is orthogonal to $\underline{v}$. These two basis vectors are related to each other through the duality relation $\underline{e}^{(i)} \cdot \underline{e}_{(j)} = \delta^i_j$ (Kronecker delta). Note also that $e^{(i)} = (e_{(j)} \times e_{(k)})/J$ and vice-verse $e_{(i)} = (e^{(j)} \times e^{(k)})J$, where the Jacobian $J \equiv \sqrt{g} = |e_{(i)} \cdot e_{(j)} \times e_{(k)}|$ represents the volume of a hexahedron formed by the vector $\underline{e}_{(i)}$.

By multiplying $\underline{e}^{(i)}$ on both hand sides of (10), we can easily transform the Faraday's equations in Cartesian coordinates (x, y, z) to its corresponding equations written in terms of the contravariant and covariant components in the curvilinear coordinate system (ξ, η, ζ). Define first $\underline{g}^i = \underline{e}^{(i)}$ for $i = 1{-}3$. The contravariant components of $\underline{H}$ can be expressed in terms

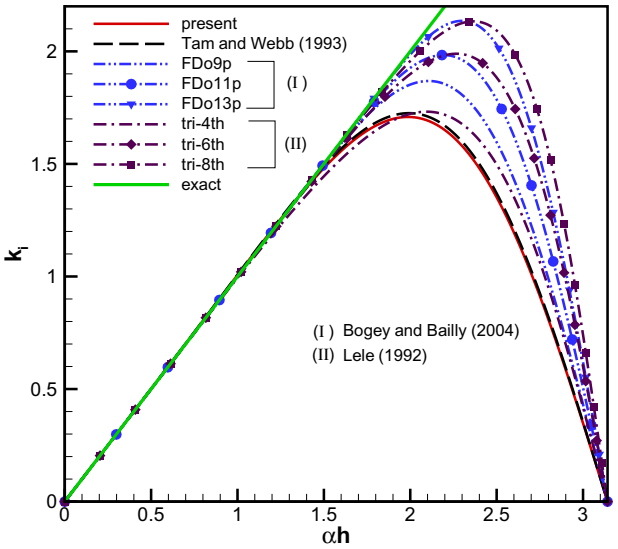

Fig. 2. Comparison of the computed values of k_i, which are plotted versus the modified wavenumber αh, among the proposed scheme (in seven stencil points), the scheme of Tam and Webb (in seven stencil points) [25], the schemes of Bogry and Bailly (in nine – thirteen stencil points) [26], and the tridiagonal compact schemes of Lele (in seven stencil points) [9].

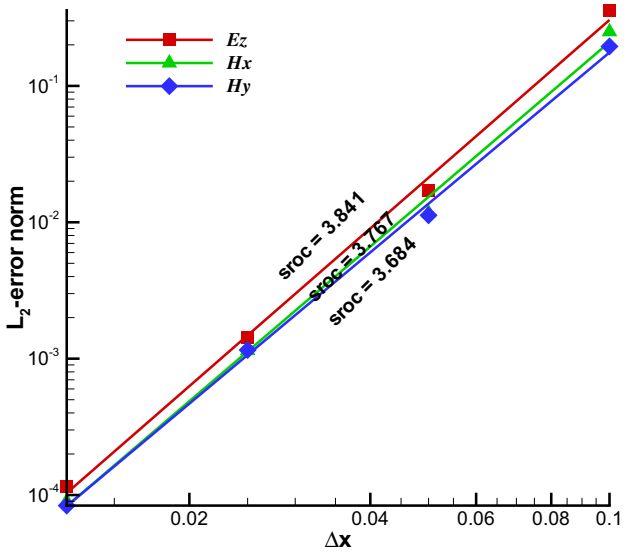

Fig. 3. The computed L_2-error norms and the corresponding spatial rates of convergence (sroc) for the three field variables.

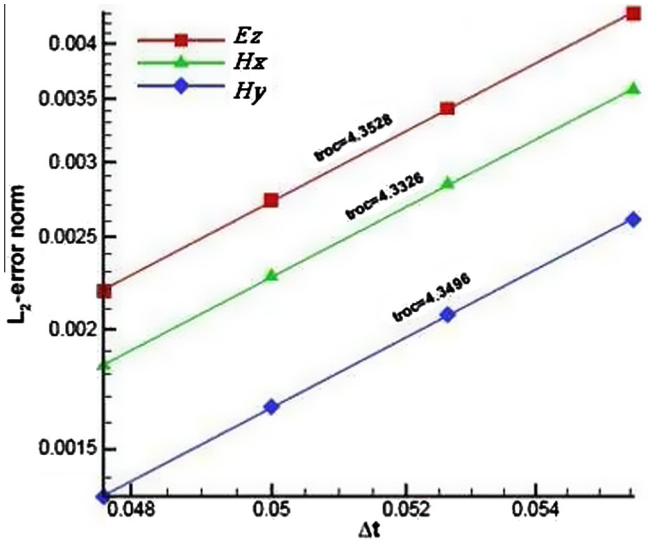

Fig. 4. The computed L_2-error norms and the corresponding temporal rates of convergence (troc) for the three field variables.

of $\underline{g}^i as (\hat{H}^1, \hat{H}^2, \hat{H}^3) \equiv \underline{H}.\underline{g}^1, \underline{H}.\underline{g}^2, \underline{H}.\underline{g}^3)$ and the covariant components of $\underline{E}$ can be expressed in terms of $\underline{g}_i$ as $(\hat{E}_1, \hat{E}_2, \hat{E}_3) \equiv \underline{E}.\underline{g}_1, \underline{E}.\underline{g}_2, \underline{E}.\underline{g}_3)$. The resulting Faraday's equations written in terms of the contravariant components of $\underline{H}$ are as follows:

$$\frac{\partial \hat{H}^1}{\partial t} = -\frac{\left(\frac{\partial \hat{E}_3}{\partial \eta} - \frac{\partial \hat{E}_2}{\partial \zeta}\right)}{\mu\sqrt{g}} - \nabla\Phi_2 \cdot \underline{g}^1, \tag{17}$$

$$\frac{\partial \hat{H}^2}{\partial t} = -\frac{\left(\frac{\partial \hat{E}_1}{\partial \zeta} - \frac{\partial \hat{E}_3}{\partial \xi}\right)}{\mu\sqrt{g}} - \nabla\Phi_2 \cdot \underline{g}^2, \tag{18}$$

$$\frac{\partial \hat{H}^3}{\partial t} = -\frac{\left(\frac{\partial \hat{E}_2}{\partial \xi} - \frac{\partial \hat{E}_1}{\partial \eta}\right)}{\mu\sqrt{g}} - \nabla\Phi_2 \cdot \underline{g}^3. \tag{19}$$

It is worthy to note here that the Faraday's equations (17)–(19) cast in curvilinear coordinates use the contravariant components of the magnetic vector in the left hand side while in the right hand side the covariant components of the electric vector are taken into account. One can also notice that the above transformed equations take almost the same form as their corresponding equations defined in Cartesian coordinates except $\underline{g}^i$ $(i = 1, 2, 3)$, which involve only the differentiation terms

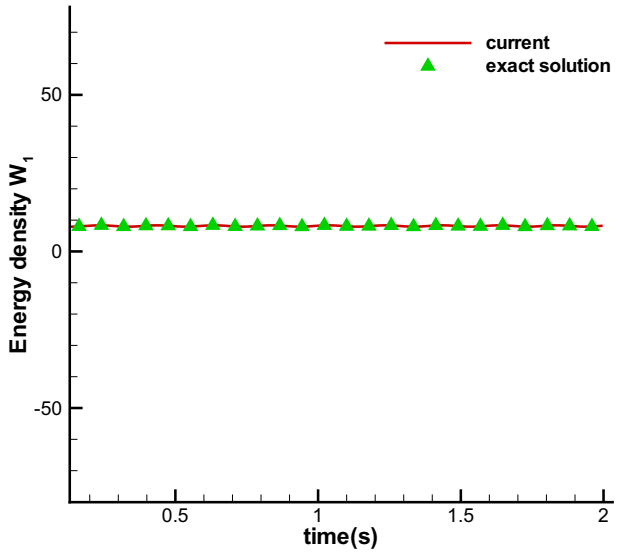

Fig. 5. The computed and exact values of the energy density, shown in (7), versus time.

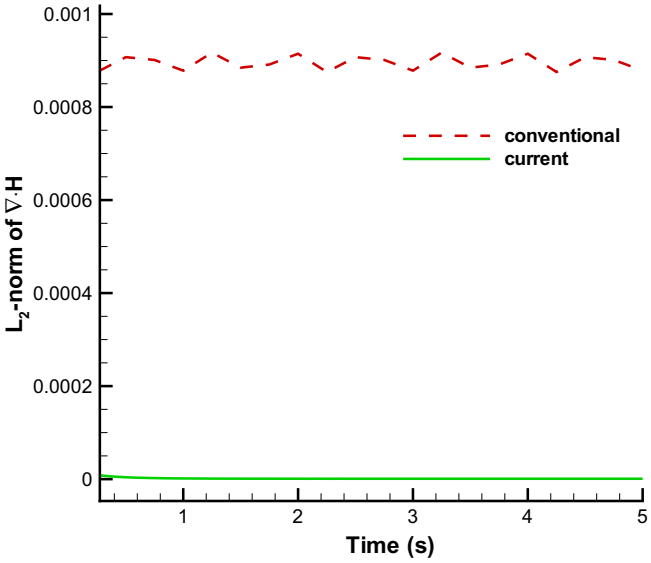

Fig. 6. Comparison of the computed L_2-norms of $\nabla \cdot \underline{H}$ versus time using the conventional and the current symplectic schemes.

Table 1
Comparison of the required CPU times using the two investigated schemes, which yield approximately the same L_2-error norms, at time $t = 10$.

Present			Yee [3]		
L_2-error norm	Grid	CPU time (s)	L_2-error norm	Grid	CPU time (s)
1.6973E−02	41 × 41	2.2969	1.5649E−02	121 × 121	4.6719
7.3012E−03	51 × 51	3.0156	6.3570E−03	189 × 189	19.0937
3.8695E−03	61 × 61	4.3438	3.1511E−03	268 × 268	56.5937

between two coordinates. Such an analogy in the two equation expressions helps to get the same prediction quality when solving the Maxwell's equations in Cartesian and curvilinear coordinates.

The Ampère's equations for the electric field $\underline{E}$ in (9) can be similarly transformed to the following equations, written in terms of the contravariant components $(\hat{E}^1, \hat{E}^2, \hat{E}^3)$ and the covariant components $(\hat{H}_1, \hat{H}_2, \hat{H}_3)$, in curvilinear coordinates

$$\frac{\partial \hat{E}^1}{\partial t} = \frac{\left(\frac{\partial \hat{H}_3}{\partial \eta} - \frac{\partial \hat{H}_2}{\partial \zeta}\right)}{\epsilon\sqrt{g}} - \nabla\Phi_1 \cdot \underline{g}^1, \tag{20}$$

$$\frac{\partial \hat{E}^2}{\partial t} = \frac{\left(\frac{\partial \hat{H}_1}{\partial \zeta} - \frac{\partial \hat{H}_3}{\partial \xi}\right)}{\epsilon\sqrt{g}} - \nabla\Phi_1 \cdot \underline{g}^2, \tag{21}$$

$$\frac{\partial \hat{E}^3}{\partial t} = \frac{\left(\frac{\partial \hat{H}_2}{\partial \xi} - \frac{\partial \hat{H}_1}{\partial \eta}\right)}{\epsilon\sqrt{g}} - \nabla\Phi_1 \cdot \underline{g}^3. \tag{22}$$

In the above, $\underline{g}^1, \underline{g}^2$ and $\underline{g}^3$ contain the information of transformation between two coordinate systems. One can find from the above transformed Ampère's equations that they are similar to those written in Cartesian coordinates provided that the contravariant components of $\underline{E}$ are used in the left hand side and the covariant components of $\underline{H}$ are used in the right hand side.

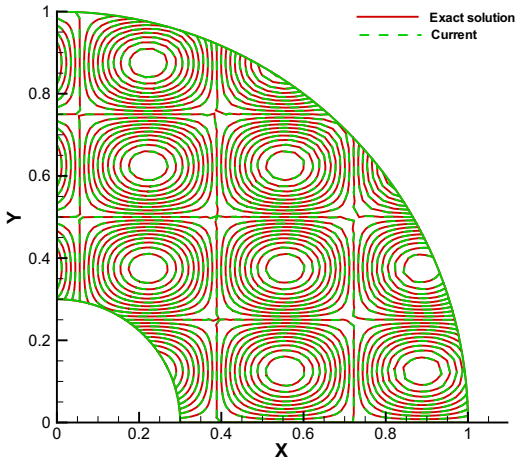

Fig. 7. Comparison of the computed and exact contours of E_z for the problem carried out in a domain of 51×51 mesh points at $t = 2$. The predicted L_2-error norm is 1.939E−3.

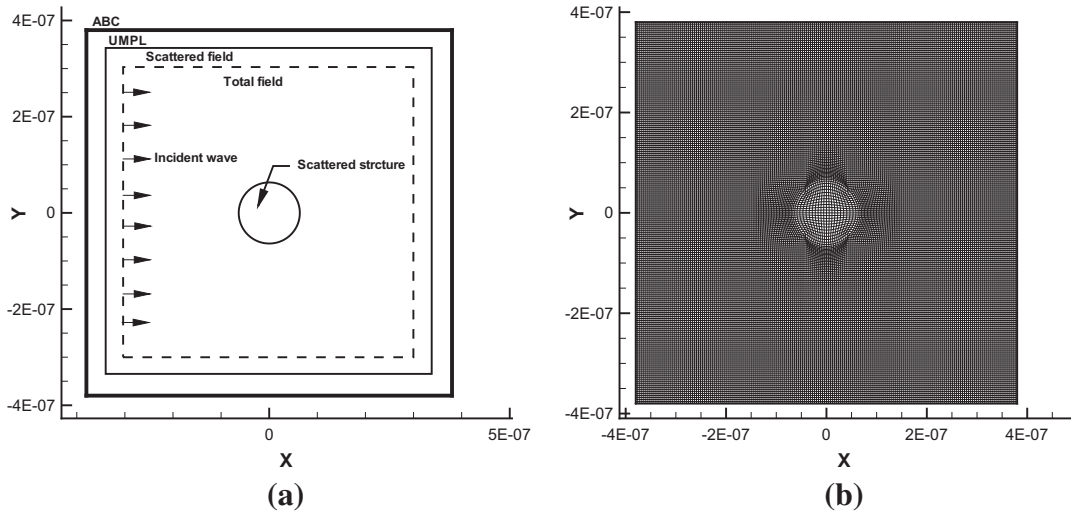

Fig. 8. Schematic of the Mie scattering problem. (a) Maxwell's equations are predicited in the total field/scattered field and the uniaxial perfectly matched layer; (b) the generated meshes.

Upon calculating the contravariant magnetic components from (17)–(19), we need to transform them to their corresponding covariant components that are needed to get the updated contravariant electric field variables. One can then transform them to their corresponding covariant components when solving Eqs. (17)–(19) for the magnetic field variables. A relationship used to calculate the contravariant components from the covariant components and vice versa involves the metric tensor $\underline{g}_{ij} \equiv \underline{e}_{(i)} \cdot \underline{e}_{(j)}$ and the inverse metric tensor $\underline{g}^{ij} \equiv \underline{e}^{(i)} \cdot \underline{e}^{(j)}$. Having computed the tensors $\underline{g}_{ij}$ and $\underline{g}^{ij}$, one can calculate the contravariant components V^i from the covariant components V_j through $V^i = \underline{g}^{ij} V_j$. Similarly, the covariant components V_j can be calculated from the contravariant components V^i by means of $V_j = \underline{g}_{ij} V^i$.

5. Maxwell's equations in uniaxial perfectly matched layer

For the problem defined in an open region, to make the numerical simulation of Maxwell's equations tackleable we need to truncate the domain by attaching a layer of absorbing medium, known as the perfectly matched layer (PML). Besides the Berenger's PML formulation [15] and the mathematically derived PML formulation [16,17], a model was also developed for the aisotropic and perfectly matched medium known as the uniaxial PML (UPML) [18,19]. We will apply it in this study to avoid the unphysical field splitting difficultly.

Maxwell's equations in UPML can be written as [18,19]

$$\frac{\partial E_x}{\partial t} = \frac{1}{\varepsilon}\left(\frac{\partial H_z}{\partial y} - \frac{\partial H_y}{\partial z} - \frac{\sigma_y}{\varepsilon_0} D_x + \frac{\sigma_x}{\varepsilon_0} D_x\right) - \frac{\sigma_z}{\varepsilon_0} E_x, \tag{23}$$

$$\frac{\partial E_y}{\partial t} = \frac{1}{\varepsilon}\left(\frac{\partial H_x}{\partial z} - \frac{\partial H_z}{\partial x} - \frac{\sigma_z}{\varepsilon_0} D_y + \frac{\sigma_y}{\varepsilon_0} D_y\right) - \frac{\sigma_x}{\varepsilon_0} E_y, \tag{24}$$

$$\frac{\partial E_z}{\partial t} = \frac{1}{\varepsilon}\left(\frac{\partial H_y}{\partial x} - \frac{\partial H_x}{\partial y} - \frac{\sigma_x}{\varepsilon_0} D_z + \frac{\sigma_z}{\varepsilon_0} D_z\right) - \frac{\sigma_y}{\varepsilon_0} E_z, \tag{25}$$

$$\frac{\partial H_x}{\partial t} = \frac{1}{\mu}\left(\frac{\partial E_y}{\partial z} - \frac{\partial E_z}{\partial y} - \frac{\sigma_y}{\varepsilon_0} B_x + \frac{\sigma_x}{\varepsilon_0} B_x\right) - \frac{\sigma_z}{\varepsilon_0} H_x, \tag{26}$$

$$\frac{\partial H_y}{\partial t} = \frac{1}{\mu}\left(\frac{\partial E_z}{\partial x} - \frac{\partial E_x}{\partial z} - \frac{\sigma_z}{\varepsilon_0} B_y + \frac{\sigma_y}{\varepsilon_0} B_y\right) - \frac{\sigma_x}{\varepsilon_0} H_y, \tag{27}$$

$$\frac{\partial H_z}{\partial t} = \frac{1}{\mu}\left(\frac{\partial E_x}{\partial y} - \frac{\partial E_y}{\partial x} - \frac{\sigma_x}{\varepsilon_0} B_z + \frac{\sigma_z}{\varepsilon_0} B_z\right) - \frac{\sigma_y}{\varepsilon_0} H_z. \tag{28}$$

The above set of equations can be transformed to their corresponding equations in the curvilinear coordinate system as follows

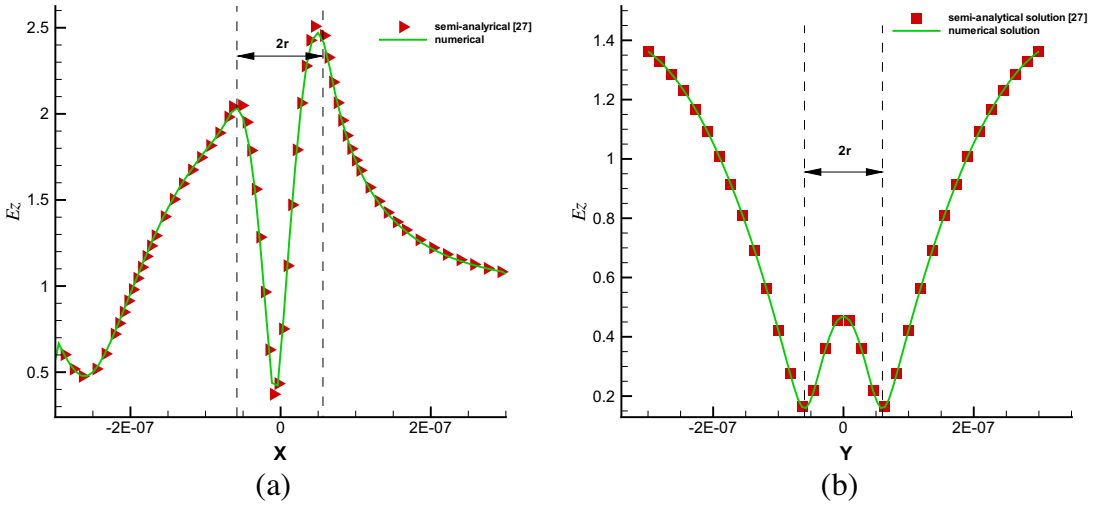

Fig. 9. Comparison of the semi-analytical and the present numerical solutions for (a) $E_z(x,0)$; (b) $E_z(0,y)$

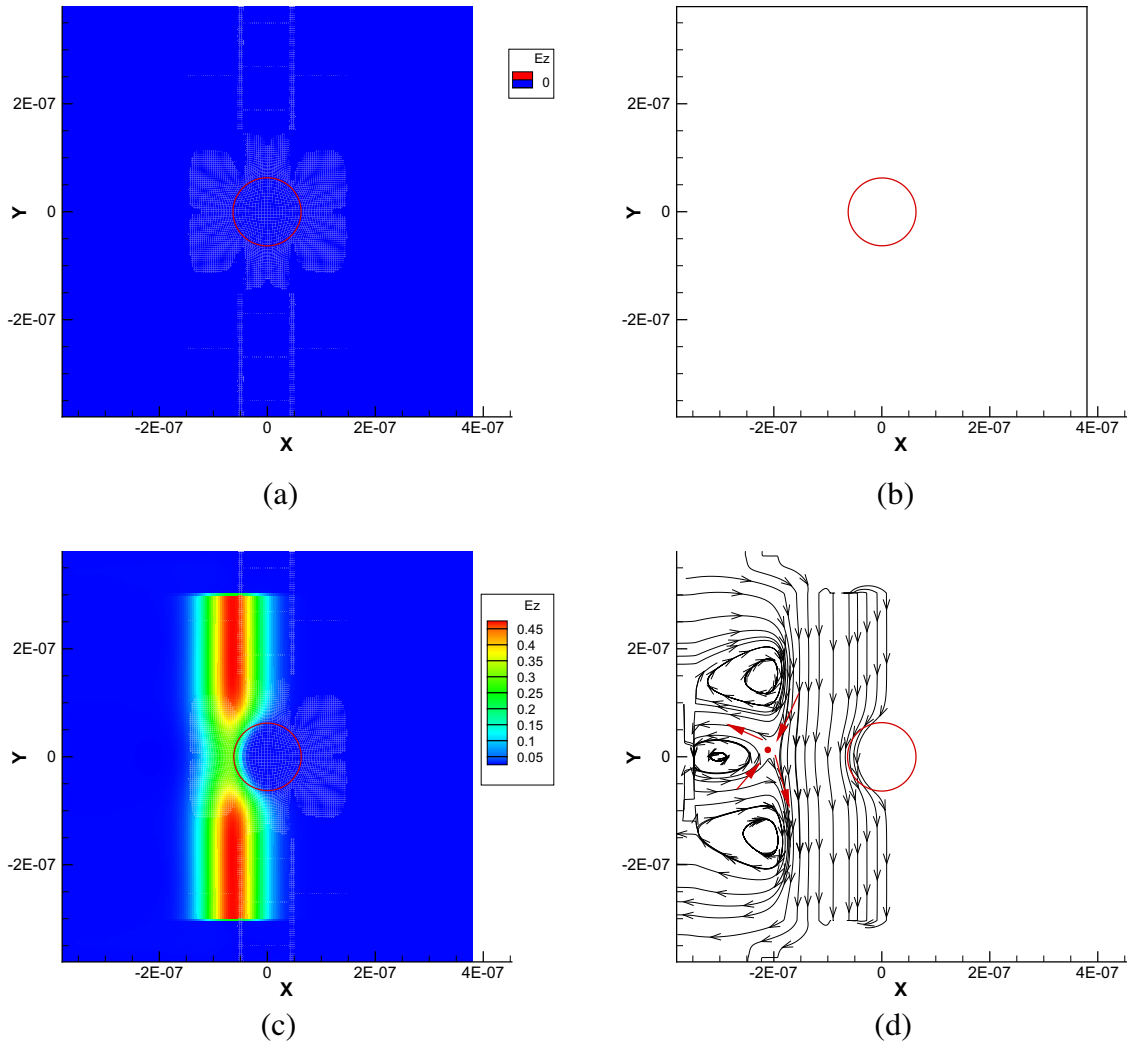

Fig. 10. Contour plots of the computed electromagnetic wave in total-field/scattered-field in a domain with a scattered structure at the time step = 0. (a) E_z-field; (b) Magnetic field lines; time step = 350; (c) E_z-field; (d) Magnetic field lines; time step = 400; (e) E_z-field; (f) Magnetic field lines; time step = 450; (g) E_z-field; (h) Magnetic field lines.

$$\frac{\partial \hat{E}^1}{\partial t} = \frac{1}{\varepsilon}\left[\frac{1}{J}\left(\frac{\partial \hat{H}_3}{\partial \eta} - \frac{\partial \hat{H}_2}{\partial \zeta}\right) - \frac{\sigma_2}{\varepsilon_0}\hat{D}_1 + \frac{\sigma_1}{\varepsilon_0}\hat{D}_1\right] - \frac{\sigma_3}{\varepsilon_0}\hat{E}^1, \tag{29}$$

$$\frac{\partial \hat{E}^2}{\partial t} = \frac{1}{\varepsilon}\left[\frac{1}{J}\left(\frac{\partial \hat{H}_1}{\partial \zeta} - \frac{\partial \hat{H}_3}{\partial \xi}\right) - \frac{\sigma_3}{\varepsilon_0}\hat{D}_2 + \frac{\sigma_2}{\varepsilon_0}\hat{D}_2\right] - \frac{\sigma_1}{\varepsilon_0}\hat{E}^2, \tag{30}$$

$$\frac{\partial \hat{E}^3}{\partial t} = \frac{1}{\varepsilon}\left[\frac{1}{J}\left(\frac{\partial \hat{H}_2}{\partial \xi} - \frac{\partial \hat{H}_1}{\partial \eta}\right) - \frac{\sigma_1}{\varepsilon_0}\hat{D}_3 + \frac{\sigma_3}{\varepsilon_0}\hat{D}_3\right] - \frac{\sigma_2}{\varepsilon_0}\hat{E}^3, \tag{31}$$

$$\frac{\partial \hat{H}^1}{\partial t} = \frac{1}{\mu}\left[\frac{1}{J}\left(\frac{\partial \hat{E}_2}{\partial \zeta} - \frac{\partial \hat{E}_3}{\partial \eta}\right) - \frac{\sigma_2}{\varepsilon_0}\hat{B}_1 + \frac{\sigma_1}{\varepsilon_0}\hat{B}_1\right] - \frac{\sigma_3}{\varepsilon_0}\hat{H}^1, \tag{32}$$

$$\frac{\partial \hat{H}^2}{\partial t} = \frac{1}{\mu}\left[\frac{1}{J}\left(\frac{\partial \hat{E}_3}{\partial \xi} - \frac{\partial \hat{E}_1}{\partial \zeta}\right) - \frac{\sigma_3}{\varepsilon_0}\hat{B}_2 + \frac{\sigma_2}{\varepsilon_0}\hat{B}_2\right] - \frac{\sigma_1}{\varepsilon_0}\hat{H}^2, \tag{33}$$

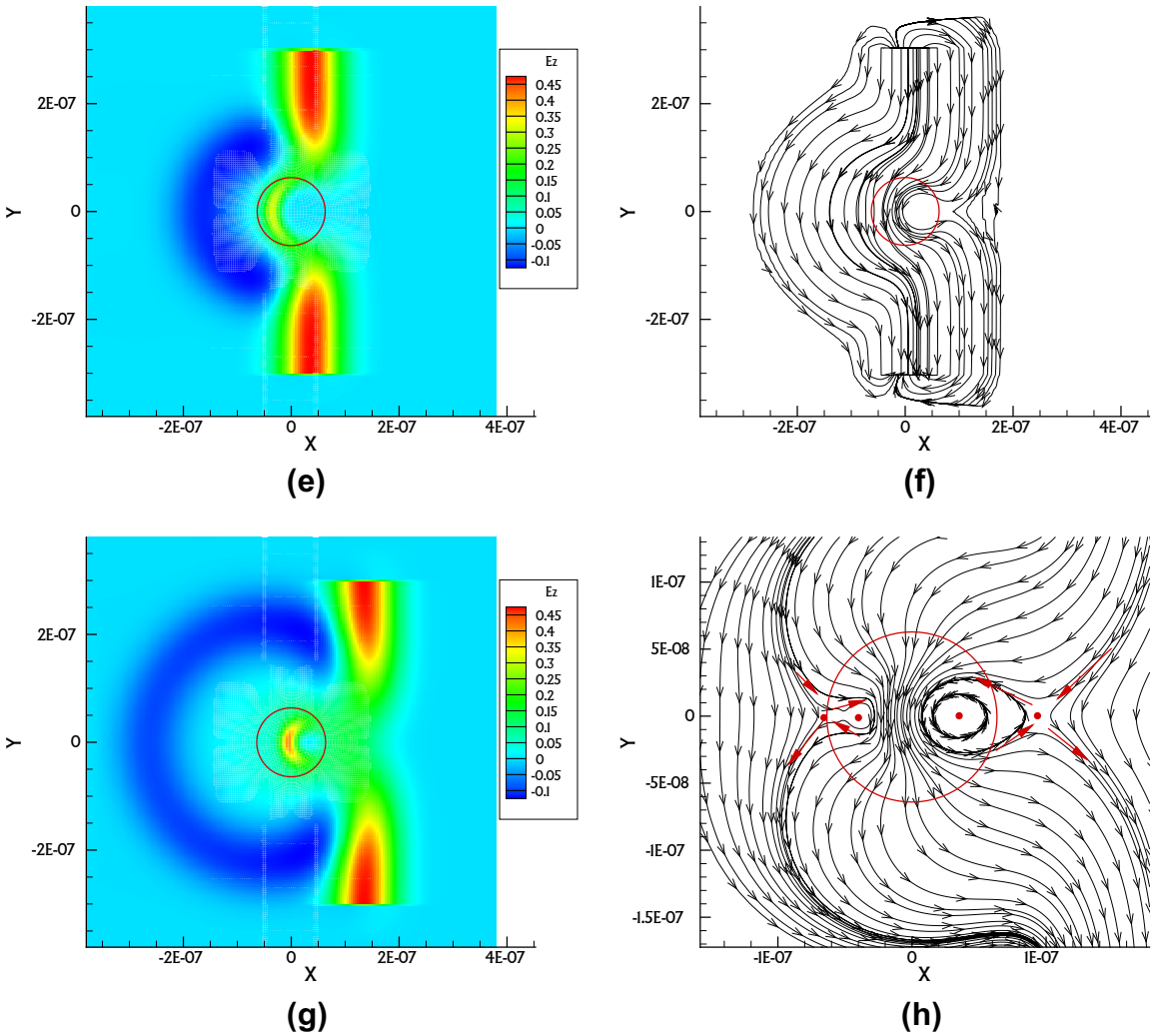

Fig. 10. (*continued*)

$$\frac{\partial \hat{H}^3}{\partial t} = \frac{1}{\mu}\left[\frac{1}{J}\left(\frac{\partial \hat{E}_1}{\partial \eta} - \frac{\partial \hat{E}_2}{\partial \xi}\right) - \frac{\sigma_1}{\varepsilon_0}\hat{B}_3 + \frac{\sigma_3}{\varepsilon_0}\hat{B}_3\right] - \frac{\sigma_2}{\varepsilon_0}\hat{H}^3. \tag{34}$$

In the above, σ_x, σ_y and σ_z denote the electric conductivities in the x, y, z dimensions while σ_1, σ_2 and σ_3 are the electric conductivities along the ξ, η, ζ coordinates in the curvilinear system.

6. Discretization method

For ease of presentation of the proposed discretization scheme, we consider the following two-dimensional Maxwell's equations in Cartesian coordinates. For the transverse magnetic polarization case, the time-evolving magnetic field $(H_x, H_y, 0)$ and the scalar electric field $(0, 0, E_z)$ are governed by

$$\begin{aligned}
\frac{\partial H_x}{\partial t} &= -\frac{1}{\mu}\frac{\partial E_z}{\partial y} - \frac{\partial \Phi_2}{\partial x}, \\
\frac{\partial H_y}{\partial t} &= \frac{1}{\mu}\frac{\partial E_z}{\partial x} - \frac{\partial \Phi_2}{\partial y}, \\
\frac{\partial E_z}{\partial t} &= \frac{1}{\epsilon}\left(\frac{\partial H_y}{\partial x} - \frac{\partial H_x}{\partial y}\right), \\
\nabla^2 \Phi_2 &= -\frac{\partial}{\partial t}\left(\frac{\partial H_x}{\partial x} + \frac{\partial H_y}{\partial y}\right).
\end{aligned} \tag{35}$$

The transformed equations in curvilinear coordinates for (35), cast in contravariant and covariant components of $\underline{H}$ and $\underline{E}$, are as follows:

$$\begin{aligned}
\frac{\partial \hat{H}^1}{\partial t} &= -\frac{1}{\mu J}\frac{\partial E_z}{\partial \eta} - \frac{1}{J^2}S_1,\\
\frac{\partial \hat{H}^2}{\partial t} &= \frac{1}{\mu J}\frac{\partial E_z}{\partial \xi} - \frac{1}{J^2}S_2,\\
\frac{\partial E_z}{\partial t} &= \frac{1}{\epsilon J}\left(\frac{\partial \hat{H}_2}{\partial \xi} - \frac{\partial \hat{H}_1}{\partial \eta}\right),\\
\nabla^2 \Phi_2 &= -\frac{\partial}{\partial t}\left\{\frac{1}{J}\left[\frac{\partial (J\hat{H}^1)}{\partial \xi} + \frac{\partial (J\hat{H}^2)}{\partial \eta}\right]\right\},
\end{aligned} \tag{36}$$

where $S_1 = (y_\eta^2 \frac{\partial \Phi_2}{\partial \xi} - y_\xi y_\eta \frac{\partial \Phi_2}{\partial \eta} + x_\eta^2 \frac{\partial \Phi_2}{\partial \xi} - x_\xi x_\eta \frac{\partial \Phi_2}{\partial \eta})$ and $S_2 = (y_\xi^2 \frac{\partial \Phi_2}{\partial \eta} - y_\xi y_\eta \frac{\partial \Phi_2}{\partial \xi} + x_\xi^2 \frac{\partial \Phi_2}{\partial \eta} - x_\xi x_\eta \frac{\partial \Phi_2}{\partial \xi})$. One can rewrite the working equations for the two chosen auxiliary variables $\rho \equiv \Phi_1$ and Φ_2 in curvilinear coordinates as follows

$$\nabla^2 \rho = \frac{1}{\sqrt{g}}\frac{\partial}{\partial \xi^i}\left(g^{ij}\sqrt{g}\frac{\partial \rho}{\partial \xi^{ij}}\right). \tag{37}$$

On examining the four equations shown in (36) we know that the quality of the predicted TM mode solutions depends on the employed flux discretization scheme. It depends also on the scheme used to calculate the values of $x_\xi, x_\eta, y_\xi, y_\eta$, which are the

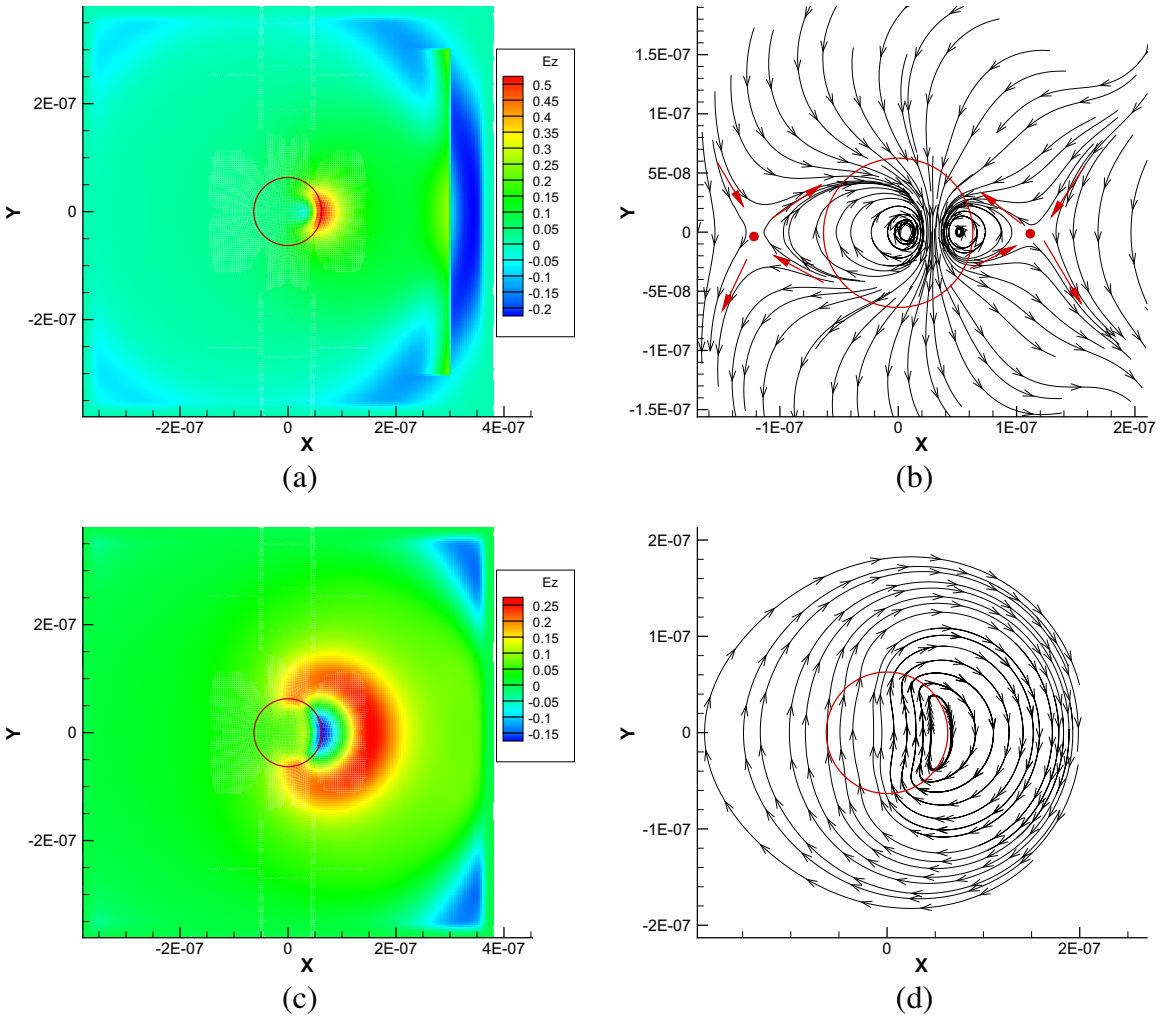

Fig. 11. Contour plots of the computed electromagnetic wave in total-field/scattered-field in a domain with a scattered structure at the time step = 550. (a) E_z-field; (b) Magnetic field lines; time step = 600; (c) E_z-field; (d) Magnetic field lines; time step = 640; (e) E_z-field; (f) Magnetic field lines; time step = 740; (g) E_z-field; (h) Magnetic field lines.

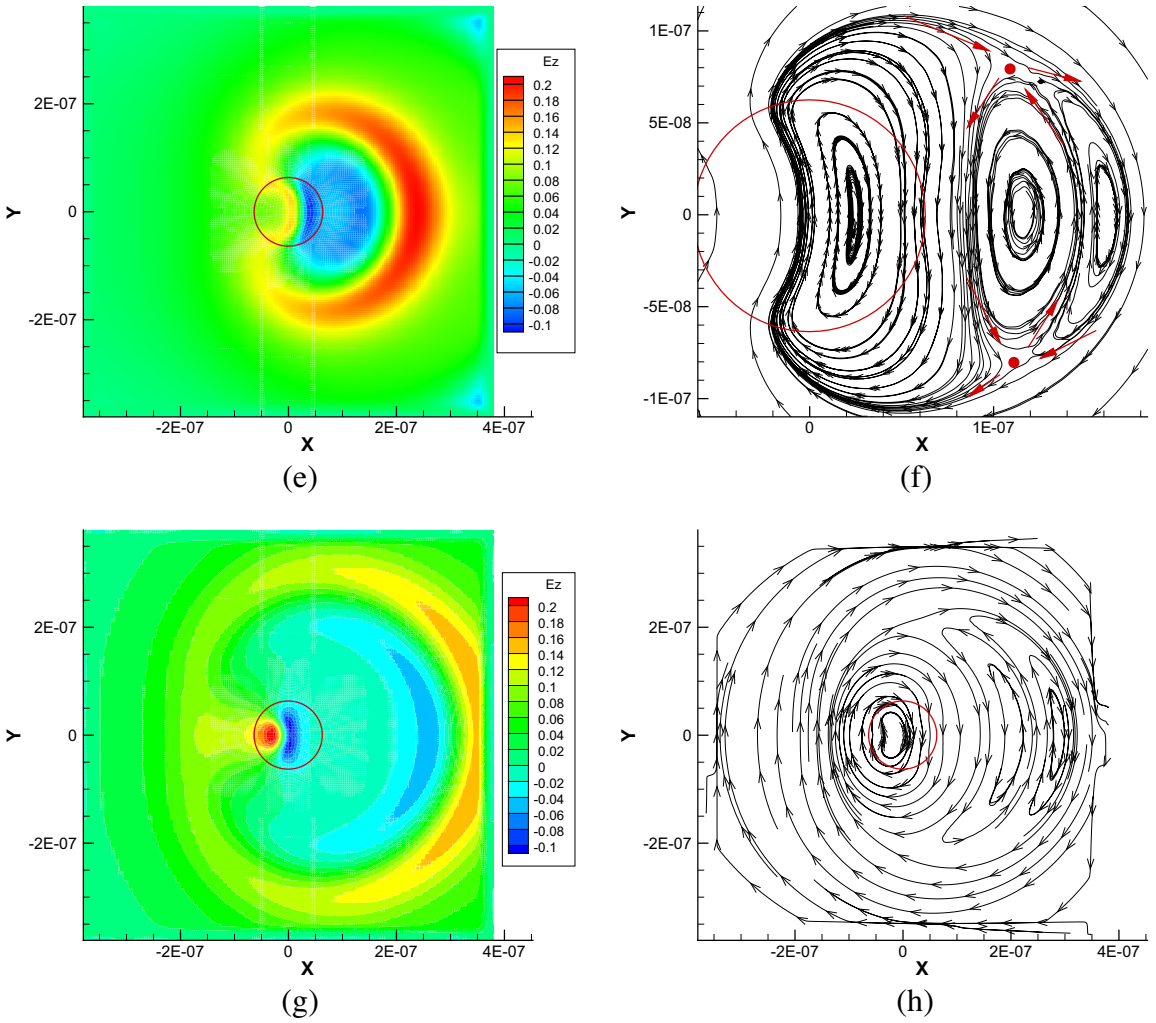

Fig. 11. (*continued*)

components in the covariant basis vector. We will present in Section 6.1 for these derivative terms that involve the transformation of equations between the two coordinate systems, in Section 6.2 for the temporal derivatives, and finally in Section 6.3 for the spatial derivative terms shown in (36).

6.1. Jacobian-preserving compact scheme

Due to the Jacobian $\frac{1}{J}\left(\equiv\frac{1}{\sqrt{g}}\right)$ shown in the transformed Maxwell's equations in (17)–(22) (29)–(34) for simple medium and in (36) for perfectly matched layer, it is essential to compute the magnitude of Jacobian. As a result, the quality of the predicted electric and magnetic field variables in complex domain depends on the computed accuracies of the components $\frac{\partial x}{\partial\xi}$, $\frac{\partial x}{\partial\eta}$, $\frac{\partial y}{\partial\xi}$, $\frac{\partial y}{\partial\eta}$ in the following Jacobian matrix $J(\equiv\frac{\partial x_i}{\partial\xi_j})$ and the determinant itself

$$|J|=\frac{\partial x}{\partial\xi}\frac{\partial y}{\partial\eta}-\frac{\partial x}{\partial\eta}\frac{\partial y}{\partial\xi}. \tag{38}$$

It has been well known that simulation quality can be considerably deteriorated by a large mesh skewness and a high aspect ratio. To avoid this problem, a rigorous means of computing the four components in the Jacobian matrix is presented below.

Let f be x and f' be $\frac{\partial x}{\partial\xi}$, for example, the value of f' at a node i is computed implicitly by the following centered compact equation so that the metric tensor term $\frac{\partial x}{\partial\xi}$, for example, can be accurately obtained in a grid of three stencil points

$$af'_{i+1,j}+f'_{i,j}+af'_{i-1,j}=\frac{b(f_{i+1,j}-f_{i-1,j})}{2h}. \tag{39}$$

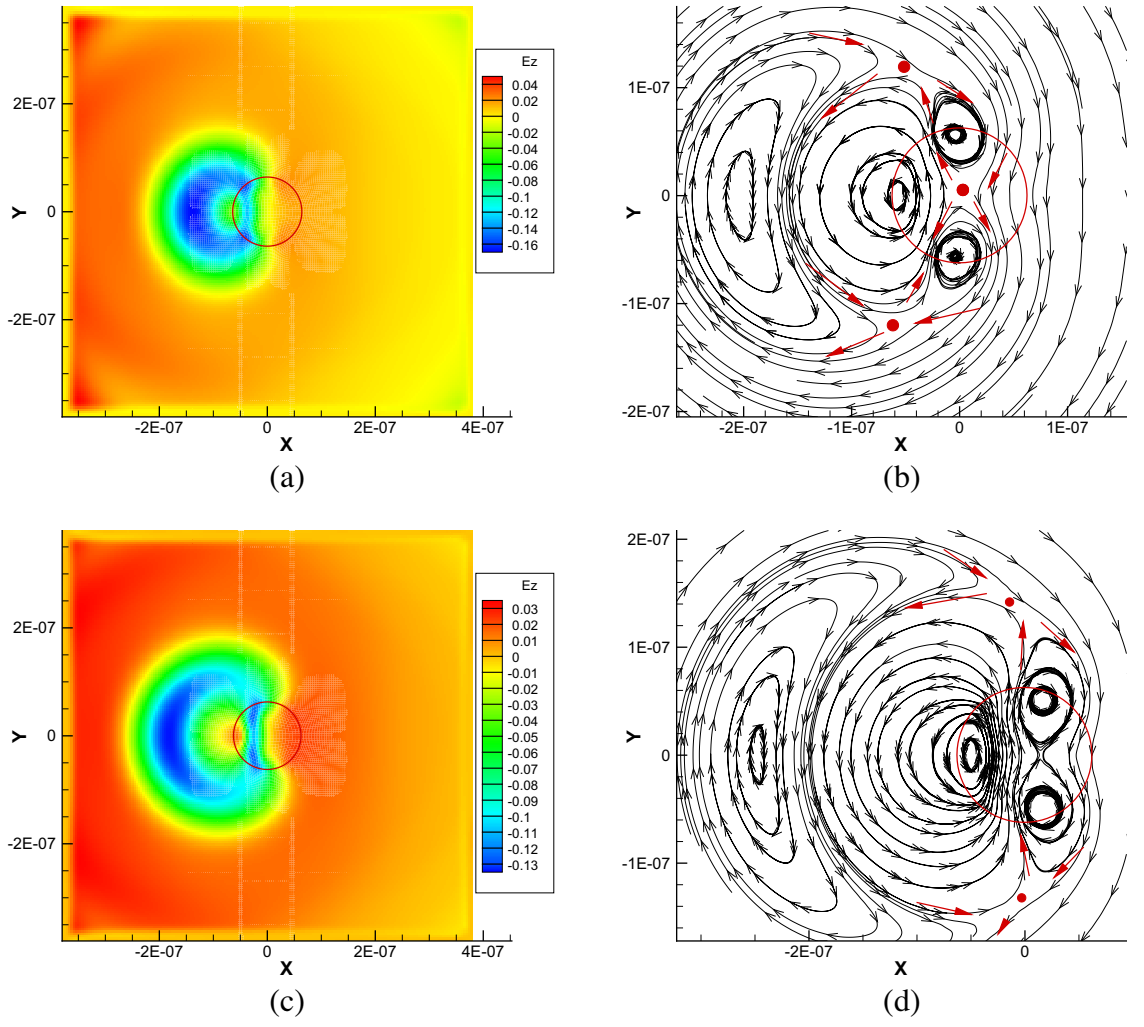

Fig. 12. Contour plots of the computed electromagnetic wave in total-field/scattered-field in a domain with a scattered structure at the time step = 840. (a) E_z-field; (b) Magnetic field lines; time step = 860; (c) E_z-field; (d) Magnetic field lines; time step = 900; (e) E_z-field; (f) Magnetic field lines; time step = 1000; (g) E_z-field; (h) Magnetic field lines.

After conducting modified equation analysis on the above discrete equation, the leading error term is eliminated to get the following algebraic equation

$$-2a + b = 1. \tag{40}$$

We can then substitute this equation into (39) to get the following equation for f_i'

$$f'_{i,j} = -a(f'_{i+1,j} + f'_{i-1,j}) + \frac{(1+2a)(f_{i+1,j} - f_{i-1,j})}{2h}. \tag{41}$$

Referring to Fig. 1, we can similarly derive the approximated expressions for $\frac{\partial x}{\partial \xi}$, $\frac{\partial x}{\partial \eta}$, $\frac{\partial y}{\partial \xi}$, $\frac{\partial y}{\partial \eta}$. The determinant of the Jacobian matrix is thus expressed as follows

$$\begin{aligned} |J(a)| &= \frac{\partial x}{\partial \xi}\frac{\partial y}{\partial \eta} - \frac{\partial x}{\partial \eta}\frac{\partial y}{\partial \xi} \\ &= [(a+0.5)(x_3 - x_1) - a(x_\xi|_3 + x_\xi|_1)] \\ &\quad \times \left[(a+0.5)(y_4 - y_2) - a(y_\eta|_4 + y_\eta|_2)\right] \\ &\quad - \left[(a+0.5)(x_4 - x_2) - a(x_\eta|_4 + x_\eta|_2)\right] \\ &\quad \times \left[(a+0.5)(y_3 - y_1) - a(y_\xi|_3 + y_\xi|_1)\right]. \end{aligned} \tag{42}$$

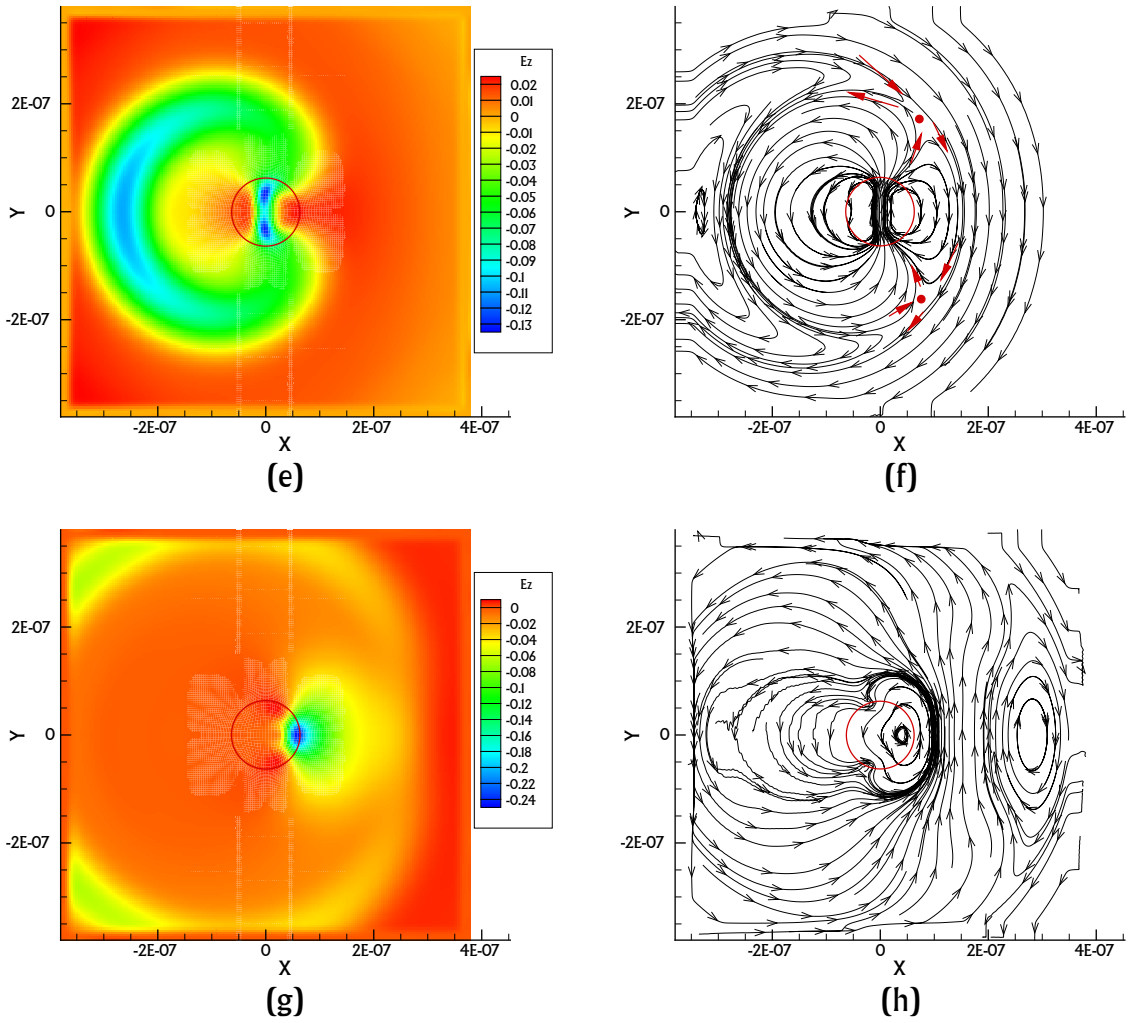

Fig. 12. (*continued*)

It is now clear that the accuracy of the determinant of Jacobian matrix depends on the free parameter a introduced in Eq. (39). For a better calculation of $\frac{\partial x}{\partial \xi}$, $\frac{\partial x}{\partial \eta}$, $\frac{\partial y}{\partial \xi}$ and $\frac{\partial y}{\partial \eta}$, in this study we underlie that the exact value of $|J|$ is the ratio of the area of the physical domain and the area of the corresponding computational domain, or

$$J_{\text{exact}} = \frac{A_{\text{physical}}}{A_{\text{computational}}}. \tag{43}$$

The area of the physical domain A_{physical} for a point at (i,j), for example, is the summation of the four areas 1–4 and the area of computational domain $A_{\text{computational}}$, which is the summation of the four areas schematic in Fig. 1. By setting $|J(a)| = |J_{\text{exact}}|$, one can determine the coefficient a for each interior grid point.

6.2. Fourth-order accurate symplecticity-preserving temporal scheme

When simulating the Hamiltonian differential equations (1,2), one in theory must apply a symplectic structurre-preserving numerical method to retain its long-term solution behavior. At the same time we demand also satisfaction of the local conservation law [12,13]. For the purpose of preserving the multisymplectic geometric structure embedded in Maxwell's equations, the symplectic integrator is employed to approximate the time derivative terms shown in the equations in (35).

The first three equations in (35) can be written as $\partial \underline{\phi}/\partial t = \underline{f}$, where $\underline{\phi} = (H_x, H_y, E_z)^T$ and $\underline{f} = \left(-\frac{1}{\mu}\partial E_z/\partial y - \partial \Phi_2/\partial x, \frac{1}{\mu}\partial E_z/\partial x - \partial \Phi_2/\partial y, \frac{1}{\epsilon}(\partial H_y/\partial x - \partial H_x/\partial y)\right)^T$. One of the representative scalar equations in $\partial \underline{\phi}/\partial t = \underline{f}$, which is given by $\partial \phi/\partial t = f$, will be approximated within the semi-discretization framework. By applying the

fourth-order accurate implicit symplectic Runge–Kutta scheme [2], the resulting coupled equations shown below can be employed to get the fourth-order temporal accuracy for the equation $\partial\phi/\partial t = f$:

$$\phi^{(1)} = \phi^n + \Delta t\left[\frac{1}{4}f^{(1)} + \left(\frac{1}{4}+\frac{1}{2\sqrt{3}}\right)f^{(2)}\right], \tag{44}$$

$$\phi^{(2)} = \phi^n + \Delta t\left[\left(\frac{1}{4}-\frac{1}{2\sqrt{3}}\right)f^{(1)} + \left(\frac{1}{4}\right)f^{(2)}\right], \tag{45}$$

$$\phi^{n+1} = \phi^n + \Delta t\left[\frac{1}{2}f^{(1)} + \frac{1}{2}f^{(2)}\right]. \tag{46}$$

In the above, $f^{(1)}$ and $f^{(2)}$ represent the values of f evaluated at $t = n + \left(\frac{1}{2}+\frac{1}{2\sqrt{3}}\right)dt$ and $t = n + \left(\frac{1}{2}-\frac{1}{2\sqrt{3}}\right)dt$, respectively. We will then approximate the remaining first-order spatial derivative terms in the Maxwell's equations.

6.3. Optimized compact scheme for the first-order derivative term

When discretizing the first-order derivative terms in non-staggered grids, we should carefully eliminate the numerical oscillations of an even–odd (or checkerboard decoupling) type. Approximation of $\partial H_x/\partial x$, for example, at an interior point (i,j) in collocated mesh system, it is essential to take the nodal value of $H_x|_{i,j}$ into consideration. Such an approximation helps not only to get rid of the so-called even–odd decoupling oscillations but also to yield better resolution properties than other conventional finite difference schemes of the comparable order of accuracy. The centered compact difference scheme proposed earlier in [20,21] is employed in a mesh of grid spacing h:

$$\left.\frac{\partial H_x}{\partial x}\right|_{i,j} = a_1 H_x|_{i+3,j} + a_2 H_x|_{i+2,j} + a_3 H_x|_{i+1,j} - a_3 H_x|_{i-1,j} - a_2 H_x|_{i-2,j} - a_1 H_x|_{i-3,j}. \tag{47}$$

The coefficients a_1, a_2 and a_3 shown above are determined by applying Taylor series expansion for $H_x|_{i\pm1,j}, H_x|_{i\pm2,j}$ and $H_x|_{i\pm3,j}$ with respect to $H_x|_{i,j}$ and, then, eliminating the first two leading error terms $\frac{\partial^2 H_x}{\partial x^2}$ and $\frac{\partial^3 H_x}{\partial x^3}$ shown in the modified equation. One more algebraic equation needs to be derived for uniquely determining the three weighting coefficients introduced in (47).

When applying the centered compact difference schemes to approximate the first-order spatial derivative terms in the currently adopted non-staggered meshes, the prediction very often suffers numerical oscillations [22]. Reduction or removal of oscillations of this type requires directly introducing a proper dissipation or adding a dissipative term implicitly through an appropriate filter [23,24]. These procedures inevitably add dissipation to the numerical scheme and can smear the physically sharp solution. This is the impetus for the development of the optimized centered compact difference scheme given below in a less explored non-staggered grid system in the area of computational electromagnetism for the elimination of numerical instability.

Instead of solely applying the truncation analysis to get the three algebraic equations for the introduced weighting coefficients in the proposed compact equation, we intend to eliminate the wave-like error and hope to get a better resolution by minimizing the dispersion error. Following the work of Tam and Webb [25], the Fourier transform and its inverse for $\frac{\partial H_x}{\partial x}$ are defined as follows

$$\tilde{H}_x(\alpha) = \frac{1}{2\pi}\int_{-\infty}^{+\infty} H_x(x)e^{-\mathbf{i}\alpha x}dx, \tag{48}$$

$$H_x(x) = \int_{-\infty}^{+\infty} \tilde{H}_x(\alpha)e^{\mathbf{i}\alpha x}d\alpha. \tag{49}$$

Fourier transform is then conducted on each term shown in Eq. (47) to get the following actual wavenumber α

$$\alpha \simeq \frac{-\mathbf{i}}{h}(a_1 e^{\mathbf{i}3\alpha h} + a_2 e^{\mathbf{i}2\alpha h} + a_3 e^{\mathbf{i}\alpha h} - a_3 e^{-\mathbf{i}\alpha h} - a_2 e^{-\mathbf{i}2\alpha h} - a_1 e^{-\mathbf{i}3\alpha h}). \tag{50}$$

In an approximation sense, the effective wavenumber $\tilde{\alpha}$ is defined as follows [25]

$$\tilde{\alpha} = \frac{-\mathbf{i}}{h}(a_1 e^{\mathbf{i}3\alpha h} + a_2 e^{\mathbf{i}2\alpha h} + a_3 e^{\mathbf{i}\alpha h} - a_3 e^{-\mathbf{i}\alpha h} - a_2 e^{-\mathbf{i}2\alpha h} - a_1 e^{-\mathbf{i}3\alpha h}), \tag{51}$$

where $\mathbf{i} = \sqrt{-1}$. To get a better dispersive approximation, the magnitude of $|\alpha h - \tilde{\alpha}h|^2$ should be very close to 0^+. The error function $E(\alpha)$ defined below is therefore minimized over the modified (or scaled) wavenumber range $-\frac{\pi}{2} \leqslant \gamma \leqslant \frac{\pi}{2}$

$$E(\alpha) = \int_{-\frac{\pi}{2}}^{\frac{\pi}{2}} |\alpha h - \tilde{\alpha}h|^2 d(\alpha h) = \int_{-\frac{\pi}{2}}^{\frac{\pi}{2}} |\gamma - \tilde{\gamma}|^2 d\gamma, \tag{52}$$

where $\gamma = \alpha h$. The positive-valued function E is minimized by enforcing the limiting condition $\frac{\partial E}{\partial a_3} = 0$ to get the third algebraic equation. The equation derived by the above minimization of modified wavenumber error is used together with the

other two algebraic equations derived previously from the modified equation analysis. By virtue of the above two underlying analyses, we can get the following three coefficients $a_i (i = 1 \sim 3)$ shown in (47)

$$a_1 = -\frac{2(3\pi - 10)}{3(15\pi - 32)}, \tag{53}$$

$$a_2 = \frac{3(9\pi - 32)}{4(15\pi - 32)}, \tag{54}$$

$$a_3 = \frac{12}{15\pi - 32}. \tag{55}$$

The proposed compact difference scheme through the minimization of numerical scaled wavenumber error has the spatial accuracy of order four

$$\frac{\partial H_x}{\partial x} = \frac{\partial H_x}{\partial x}|_{\text{exact}} - \frac{9(5\pi - 16)}{10(15\pi - 32)} h^4 \frac{\partial^5 H_x}{\partial x^5} + O(h^6) + \cdots \tag{56}$$

Analysis of the proposed spatial scheme starts from defining the coefficients k_i and k_r for the respective dispersion and dissipation errors as $k_i = \Re[\tilde{\alpha}h]$ and $k_r = \Im[\tilde{\alpha}h]$. $\Re[\tilde{\alpha}h]$ denotes the real part of $\tilde{\alpha}h$ and $\Im[\tilde{\alpha}h]$ stands for the imaginary part of $\tilde{\alpha}h$ for the proposed scheme. It is worthy to note that the value of k_r is always equal to zero because of the symmetric stencil points used in the centered compact difference scheme. In Fig. 2, the predicted values of k_i are plotted with respect to the modified wavenumber αh. For the sake of comparison, we also plot the values of k_i for the schemes of Tam and Webb [25], Lele [9], and Bogry and Bally [26].

7. Numerical results

The dual-preserving scheme formulated in non-staggered grids for simulating the TM wave is verified first by solving the Maxwell's equations that are amenable to the analytic solution. This problem solved at $\mu = 1$ and $\epsilon = 1$ in $-1 \leqslant x \leqslant 1,\ -1 \leqslant y \leqslant 1$ has the following divergence-free initial solutions $E_z(x, y, 0) = sin(3\pi x)sin(4\pi y)$, $H_x(x, y, 0) = -\frac{4}{5}cos(3\pi x)cos(4\pi y)$, $H_y(x, y, 0) = -\frac{3}{5}sin(3\pi x)sin(4\pi y)$. The resulting exact solutions for Eqs. (1,2) are as follows [2]

$$\begin{aligned} E_z(x, y, t) &= sin(3\pi x - 5\pi t)\, sin(4\pi y), \\ H_x(x, y, t) &= -\frac{4}{5} cos(3\pi x - 5\pi t)\, cos(4\pi y), \\ H_y(x, y, t) &= -\frac{3}{5} sin(3\pi x - 5\pi t)\, sin(4\pi y). \end{aligned} \tag{57}$$

Two sets of calculations are performed to get the spatial and temporal rates of convergence. Calculations are first performed at $\Delta t = 1/5000$, which is smaller than the finest grid of spacings $\Delta x = \Delta y = 1/20, 1/30, 1/40, 1/50$. The predicted errors cast in L_2-error norms are plotted in Fig. 3, from which the spatial rate of convergence is numerically predicted to be

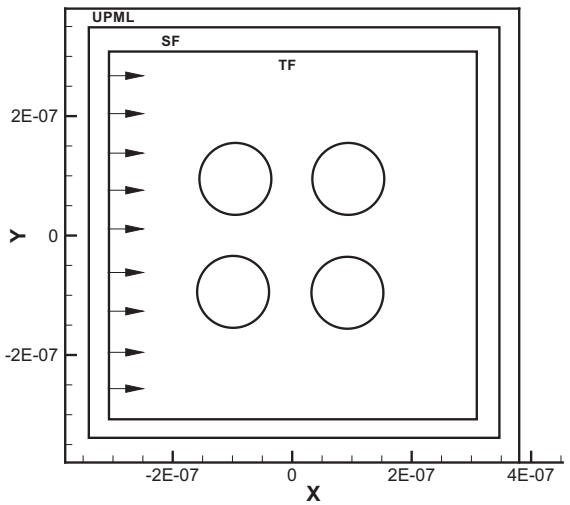

Fig. 13. Schematic of the four isotropic cylinders in physical domain.

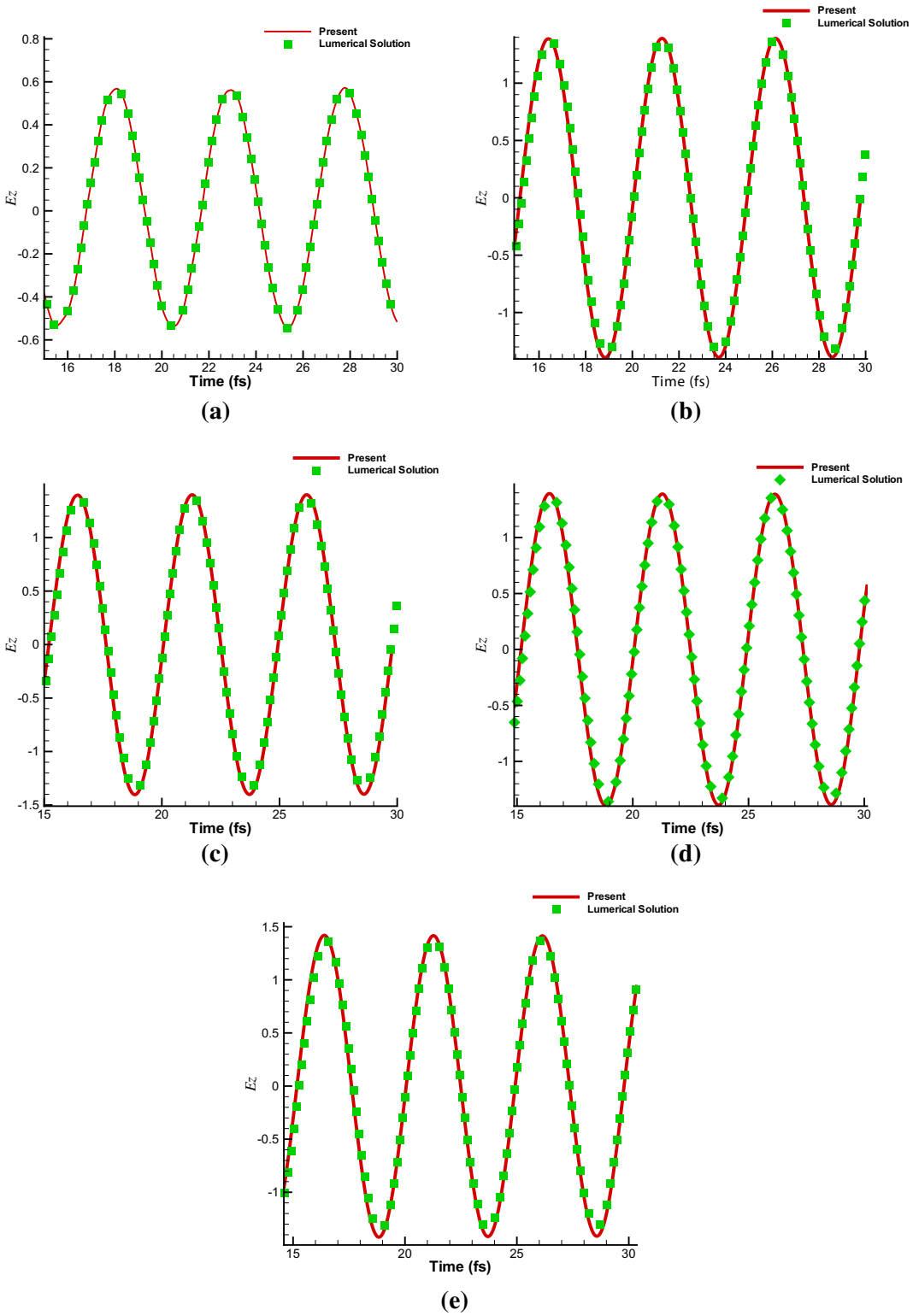

Fig. 14. Comparison of the current and Lumerical FDTD results for Ez at five different locations (x, y). (a) (0 nm, 0 nm); (b) (272 nm, 272 nm); (c) (272 nm, 480 nm); (d) (480 nm, 272 nm); (e) (480 nm, 480 nm).

fourth. The second set of calculations is performed similarly at the fixed grid spacing $\Delta x = \Delta y = 1/50$, which is smaller than the smallest chosen time interval of $\Delta t = 1/18, 1/19, 1/20, 1/21$, so that we can calculate the temporal rate of convergence. As Fig. 4 shows, the L_2-error norms decrease with the reduced time interval Δt at an approximated rate of fourth.

For the purpose of justifying the proposed scheme, the Hamiltonian defined in (6) and the energy density given in (7) are calculated. Since the Hamiltonian is trivially equal to zero for the two dimensional TM-mode Maxwell's equations, we only plot the predicted and exact values of the energy density W_1 versus time. In Fig. 5. one can clearly see that the computed value of W_1 is not varied with time. One can clearly see in Fig. 6 that the magnetic field is indeed discretely divergence-free in a domain of 51×51 grid points. We also compare the required CPU times capable of getting the similar L_2-error norms in Table 1. Based on this comparison study we know from the tabulated results that the current non-staggered scheme performs much more effectively than the Yee scheme implemented in staggered grids.

We then solve the TM-mode Maxwell's equations cast in curvilinear coordinates in a domain as shown schematic in Fig. 7. This problem is solved at $\mu = \epsilon = 1$ for the case with the specified exact boundary value according to (57). For H_x, H_y and $\nabla \cdot \underline{H}$, these values are obtained as 1.939E−3, 1.283E−3, 1.909E−3 and 1.791E−5, respectively. In the uniformly discretized domain with 51×51 grid points, the predicted solutions at $t = 2$ s are seen to agree well with the exact solution.

Furthermore, we verify the dual-preserving solver by solving the classical Mie scattering problem in curvilinear coordinates. In Fig. 8(a), a plane wave of wavelength $\lambda = 632.8$ nm is incident on the isotropic cylinder of radius $63.28nm$. For preventing wave being reflected back to the physical domain Ω $[-380, 380]$ nm from the truncated boundary Γ, the domain is divided into the total-field and the scatter-field (TF/SF). One region contains the total field (i.e. the sum of the incident field and the scattered field) while the other region contains only the scattered field. In addition, an uniaxial perfectly matched layer (UPML) is attached to the truncated boundary lines, within which the Maxwell's equations shown in (29)–(34) with the absorbing ability are solved in the 190×190 curvilinear grid system as shown schematic in Fig. 8(b). The computed values of E_z along the x-axis and y-axis in Fig. 9 show good agreement with the exact solutions. For the sake of completeness, we also plot in Figs. 10–12 the simulated time evolving contours of E_z and the magnetic field lines. One can clearly see that the originally planar incident wave becomes curved as the wave approaches the scatter.

After successfully simulating the Mie scattering problem, the proposed solver for Maxwell's equations is applied to predict the incident *EM* wave propagating in a geometrically more complex domain. Four isotropic cylinders of the same radius 63.28 nm are placed in the physical domain as shown schematic in Fig. 13, which involves as before the UPML absorbing layer. The results shown in Fig. 14, which plots $Ez(x, y, t)$ at the locations $(x, y) = (0\text{ nm}, 0\text{ nm})$, $(272\text{ nm}, 272\text{ nm})$, $(272\text{ nm}, 480\text{ nm})$, $(480\text{ nm}, 272\text{ nm})$ and $(480\text{ nm}, 480\text{ nm})$, are compared with other numerical results computed by Lumerical Solutions (http://www.lumerical.com). Good agrement between the two sets of numerical results confirms the applicability of the currently proposed solver to predict wave propagation in the curvilinear coordinate system as shown schematically in Fig. 14.

8. Conclusions

A centered compact difference scheme for the approximation of first-order spatial derivative terms shown in TM-mode Maxwell's equations has been developed in collocated curvilinear grids. The contravariant and covariant components for both electric and magnetic vectors are chosen altogether to transform the Maxwell's equations in Cartesian coordinates to the equations in curvilinear coordinates. The resulting transformed equations involving both of the contrvariant and covariant variables take almost the same form as the Cartesian Maxwell's equations. As a good discretization scheme, the symplectic and conserved properties embedded in the Maxwell's equations should be retained discretely all the time. This is the reason of employing the symplectic time integrator to preserve Hamiltonian structure in Maxwell's equations and developing compact difference scheme with the optimized numerical wavenumber characteristics for the first-order spatial derivative terms. The fourth-order accurate divergence-free Maxwell's solutions are also shown to computationally satisfy the Gauss' law for magnetism and electricity. In the current non-staggered grid approach, to compensate for the omitted Gauss's laws two modified Maxwell's equations are investigated and they are assessed as well. Several analytic and benchmark problems have been solved and the predicted solutions have good agreement with the exact and other referenced solutions.

Acknowledgements

This work was supported by the National Science Council of the Republic of China under Grants NSC96-2221-E-002–293-MY2, NSC96-2221-E-002-004 and CQSE97R0066-69. The authors also thank the anonymous reviewer for his useful comments and constructive suggestions.

References

[1] C.K. Birdsall, A.B. Langdon, Plasmas Physics via Computer Simulation, McGraw Hill, New York, 1985.
[2] J.X. Cai, Y.S. Wang, B. Wang, B. Jiang, New multisymplectic self-adjoint scheme and its composition scheme for the time-domain Maxwell's equations, J. Math. Phys. 47 (2006) 1–18.
[3] K.S. Yee, Numerical solution of initial boundary value problems involving Maxwell's equations in isotropic media, IEEE Trans. Antennas. Propag. AP4 (1996) 302–307.

[4] C.D. Munz, P. Omnes, R. Schneider, E. Sonnendrücker, U. Vo, Divergence correction techinques for Maxwell solvers based on a hyperbolic model, J. Comput. Phys. 161 (2000) 484–511.
[5] B. Cockburn, F. Li, C.W. Shu, Locally divergence-free discontinuous Galerkin methods for the Maxwell equations, J. Comput. Phys. 194 (2004) 588–610.
[6] D. Gottlieb, S.A. Orszag, Numerical Analysis of Spectral Methods, SIAM, Philadelphia, 1977.
[7] C. Canuto, M.Y. Hussaini, A. Quarteroni, T.A. Zang, Spectral Methods in Fluid Dynamics, Springer-Verlag, New York, 1987.
[8] Z. Kopal, Numerical Analysis, second ed., Wiley, New York, 1961.
[9] S.K. Lele, Compact finite difference schemes with spectral-like resolution, J. Comput. Phys. 103 (1992) 16–42.
[10] T.J. Bridges, S. Reich, Multi-symplectic integration numerical scheme for Hamiltonian PDEs that conserves symplecticity, Phys. Rev. Lett. A 284 (2001) 184–193.
[11] L.H. Kong, J.L. Hong, J.J. Zhang, Splitting multisymplectic integrators for Maxwell's equations, J. Comput. Phys. 229 (2010) 4259–4278.
[12] N. Anderson, A.M. Arthurs, Helicity and variational principles for Maxwell's equations, Int. J. Electr. 54 (1983) 861–864.
[13] F. Assous, P. Degond, E. Heintze, P.A. Raviart, J. Segre, On a finite-element method for solving the three-dimensional Maxwell equations, J. Comput. Phys. 109 (1993) 222–237.
[14] C. Greif, D. Li, D. Schötzau, X. Wei, A mixed finite element method with exactly divergence-free velocities for incompressible magnetohydrodynamics, Comput. Methods Appl. Mech. 199 (2010) 2840–2855.
[15] J.P. Berenger, A perfectly matched layer for the absorption of electromagnetic waves, J. Comput. Phys. 114 (1994) 185–200.
[16] S. Abarbanel, D. Gottlieb, On the construction and analysis of absorbing layers in CEM, Appl. Numer. Math. 27 (1998) 331–340.
[17] S. Abarbanel, D. Gottlieb, J.S. Hesthaven, Non-linear PML equations for time dependent electromagnetics in three dimensions, J. Sci. Comput. 28 (2006) 125–136.
[18] Z.S. Sack, D.M. Kingsland, R. Lee, J.F. Lee, A perfectly matched anisotropic absorber for use as an absorbing boundary condition, IEEE Trans. Antennas. Propag. 43 (1995) 1460–1463.
[19] S.D. Gedney, An anisotropic perfectly matched layer-absorbing medium for the truncation of FDTD lattices, IEEE Trans. Antennas. Propag. 44 (1996) 1630–1639.
[20] T.W.H. Sheu, R.K. Lin, An incompressible Navier–Stokes model implemented on nonstaggered grids, Numer. Heat Trans. B Fundam. 44 (2003) 277–294.
[21] P.H. Chiu, T.W.H. Sheu, R.K. Lin, Development of a dispersion-relation-preserving upwinding scheme for incompressible Navier–Stokes equations on non-staggered grids, Numer. Heat Trsnd. B Fundam. 48 (2005) 543–569.
[22] A. Shah, L. Yuan, A. Khan, Upwind compact finite difference scheme for time-accurate solution of the incompressible Navier–Stokes equations, Appl. Math. Comput. 215 (2010) 3201–3213.
[23] D.V. Gaitonde, J.S. Shang, J.L. Young, Practical aspects of high-order numerical schemes for wave propagation phenomena, Int. J. Numer. Methods Eng. 45 (1999) 1849–1869.
[24] J.P. Boyd, Chebyshev and Fourier Spectral Methods, second ed., Dover Publications, Inc., Mineola, New York, 2000.
[25] C.K.W. Tam, J.C. Webb, Dispersion-relation-preserving finite difference schemes for computational acoustics, J. Comput. Phys. 107 (1993) 262–281.
[26] C. Bogry, C. Bailly, A family of low dispersive and low dissipative explicit schemes for flow and noise computations, J. Comput. Phys. 194 (2004) 194–214.